Fourth-order Coronagraph for High-contrast Imaging of Exoplanets with Off-axis Segmented Telescopes

Satoshi Itoh[1] and Taro Matsuo[2,3]

[1] Department of Earth and Space Science, Graduate School of Science, Osaka University, 1-1, Machikaneyama-cho, Toyonaka, Osaka 560-0043, Japan
[2] Department of Physics, Graduate School of Science, Nagoya University, Furo-cho, Chikusa-ku, Nagoya, Aichi, 464-8602, Japan
[3] NASA Ames Research Center, Moffett Field, CA 94035, USA

Abstract

We propose a coronagraphic system with fourth-order null for off-axis segmented telescopes, which is sufficiently insensitive to the telescope pointing errors and finite angular diameter of the host star to enable high-contrast imaging of potentially habitable planets. The inner working angle of the coronagraphic system is close to $1\lambda/D$, and there is no outer limit. The proposed coronagraphic system is made up of a new focal plane mask and an optimized Lyot stop with the second-order null. The new focal plane mask is an extension of the band-limited masks with a phase modulation. We construct a coronagraphic system with fourth-order null by placing two of the new coronagraph systems in succession to be orthogonal to each other. The proposed system is limited to narrow-band usage. The characteristics of the proposed coronagraph system are derived analytically, which includes (1) the leak of stellar lights due to the finite stellar diameter and pointing jitter of a telescope, and (2) the peak throughput. We achieve the performance simulations of this coronagraphic system based on these analytical expressions, considering a monochromatic light of 0.75 μm and an off-axis primary mirror with a diameter of 8.5 m. Thanks to the wide working area of the mask, the result shows that terrestrial planets orbiting K and G dwarfs can be detected under the condition that the telescope pointing jitter is less than $0.01\lambda/D \approx 240$ as. The proposed coronagraphic system is promising for the detection of potentially habitable planets with future space off-axis hexagonally segmented telescopes.

Unified Astronomy Thesaurus concepts: Exoplanet detection methods (489); Direct imaging (387); Exoplanet astronomy (486); Coronagraphic imaging (313); Astronomical techniques (1684); Observational astronomy (1145); Pointing accuracy (1271); Pointing error (1272); Astrobiology (74); Exoplanets (498); Habitable planets (695); Biosignatures (2018)

1. Introduction

The data from the Kepler space telescope (Borucki 2017) has showed that about one-third of all M-dwarfs have terrestrial planets (Howard et al. 2012). After the success of the Kepler, some terrestrial planets orbiting M-dwarfs in the habitable zone of their host stars have been found by ground-based telescopes (e.g., Anglada-Escudé et al. 2016; Gillon et al. 2016). The Transiting Exoplanet Survey Satellite (TESS; Ricker et al. 2015) is expected to detect such a potentially habitable planet orbiting nearby M-dwarfs. The next step is the characterization of the atmosphere of the potentially habitable planets using a spectroscope. The prediction of features in the planet spectra has attracted a lot of debate from an astrobiological perspective (Angel et al. 1986; Kaltenegger 2017; Catling et al. 2018; Fujii et al. 2018; Kiang et al. 2018; Meadows et al. 2018; Schwieterman et al. 2018). At mid-infrared wavelength, the non-thermal equilibrium of the atmospheres due to biological activity can be investigated from the thermal emission and transmission spectra. The highly stable spectrophotometry (Matsuo et al. 2016; Itoh et al. 2017; Goda & Matsuo 2018) and the nulling space interferometer (Bracewell & MacPhie 1979; Angel & Woolf 1997; Matsuo et al. 2011) have been developed for this purpose. In the visible and the near-infrared wavelength range, reflection spectra of potentially habitable exoplanets can be examined using high-contrast imaging with an external occulter (Copi & Starkman 2000; Cash 2006; Vanderbei et al. 2007) or coronagraph.

Among these proposed methods, the most diverse is the coronagraphic methods (e.g., Roddier & Roddier 1997;

Rouan et al. 2000; Kuchner & Traub 2002; Foo et al. 2005; Guyon et al. 2005; Mawet et al. 2005). However, most of the coronagraphs operate for only monolithic pupils without discontinuities. This non-ideality of the coronagraphic performance with respect to pupil discontinuities becomes a significant problem when these coronagraphs are applied to the segmented telescopes. This is because the planet-to-star contrast is 10^{-10} or 10^{-8} for a G- or M-type dwarf in visible light.

Several researches have been carried out on the problem of pupil discontinuities to detect the potentially habitable planets. For example, Sivaramakrishnan & Yaitskova (2005) studied and examined the performance of a Lyot-type coronagraph for a monochromatic point source with off-axis apertures segmented by gaps of square lattice. According to their study, the segmentation of telescopes limits the contrast to $4g^2$ times the point-spread function before coronagraph, where g is the width of the gap normalized by the diameter of each segment. Soummer (2005) proposed the method of the apodized complex mask Lyot coronagraph (APLC). This method theoretically provides the complete null of a point source in monochromatic light with the small inner working angle for any aperture shape. There have been several performance improvements in APLC designs for obscured, segmented apertures in the last few years (e.g., N'Diaye et al. 2016). Guyon et al. (2010) proposed the application of the phase-induced amplitude apodization (PIAA; Guyon et al. 2005) to the APLC. This method is referred to as the PIAA complex mask coronagraph (PIAA-CMC). According to the result of the

numerical simulation, an ideal PIAA-CMC appears to have second-order sensitivity to the telescope pointing jitter and the finite angular size of the host star (Belikov et al. 2018). Ruane et al. (2018) proposed a numerically optimized apodization pattern of a vortex mask coronagraph for off-axis segmented telescopes. In their methods, an on-axis point source cannot be completely nulled across the focal plane. In the numerical simulation, the stellar leakage can be swept out outside the angular radius of $20\lambda/D$ to make a dark region on focal plane. The APLC, PIAA-CMC, and vector vortex coronagraphs each have manufactured prototypes and lab demonstrations in progress in broadband light (Mazoyer et al. 2019). In addition, the visible nulling coronagraph (e.g., Hicks et al. 2016) is another alternative coronagraph solution for segmented apertures.

In this paper, we propose a coronagraphic system with the fourth-order null. Our proposed system is effective for off-axis segmented telescopes such as the Large UV/optical/infrared surveyor (LUVOIR; Bolcar et al. 2018) and the Origins Space Telescope (Leisawitz et al. 2018). The proposed coronagraphic system with the fourth-order null is sufficiently insensitive to telescope pointing errors and finite stellar diameter, enabling high-contrast imaging of potentially habitable planets. Moreover, the inner working angle of the mask is close to $1\lambda/D$, and no outer edges exist. In this paper, we define the inner working angles as off-axis angles at which the peak throughput reaches the first peaks from the inside. The key element of the coronagraphic system is the new focal plane mask. The new focal plane mask is an extension of the band-limited mask coronagraph (BLMC; Kuchner & Traub 2002). The BLMC is a mask that controls only the modulus of the complex amplitude of light. This type of mask ideally works for only monolithic telescopes. However, the proposed coronagraphic mask introduces π radian phase modulation to the BLMC. Even when used with an unobscured segmented telescope, the stellar light on the re-imaged pupil after the new focal plane mask is completely nulled over the original pupil aperture. The proposed coronagraphic system is comprised of a new focal plane mask and a Lyot stop optimized for an unobscured segmented telescope. The coronagraphic system produces a second-order null. The fourth-order version of this coronagraph is constructed by placing the two second-order null coronagraphic systems in succession so as to be orthogonal to each other. This concept of the proposed coronagraphic system with fourth-order null is ideally effective to detect the potentially habitable planets with future off-axis hexagonally segmented space telescopes.

In Section 2, we present the concept of the proposed coronagraphic system, which is optimized for the unobscured off-axis segmented telescopes. In Section 3, we use the analytical expressions derived in Section 2 to calculate the habitable planet signal and host star leakage on the new coronagraph mask assuming the LUVOIR-b architecture (Gong et al. 2019). In Section 4, we discuss the extension of the new coronagraphic system to the polychromatic light and the prospect for manufacturing.

2. Theory

In this section, we review the principle of the BLMC and describe a new coronagraph system for the unobscured off-axis segmented telescope. The symbols used in this paper are summarized in Table 1.

Table 1
Notation of Symbols

Symbol	Meaning
λ	Wavelength of light
D	Effective diameter of the telescope
D_α, D_β	α- or β-directional aperture full width of the telescope
$\boldsymbol{x} = (x, y)$	Focal-plane angular coordinate normalized by λ/D
$\boldsymbol{\alpha} = (\alpha, \beta)$	Pupil-plane coordinate normalized by D
γ	Absolute value of the telescope's pointing deviation
$\delta(x)$	Dirac's delta function
$\text{rect}(x)$	$\text{rect}(x) = (1 \;\; (\lvert x \rvert \leqslant 0.5),\ 0.5 \;\; (\lvert x \rvert = 0.5),\ 0 \;\; (\lvert x \rvert \geqslant 1)$
$f * g$	Convolution of functions, f and g
$\tilde{f}$	Fourier conjugate of a function, f
$\text{Supp}(f)$	$\{\boldsymbol{x} \lvert f(\boldsymbol{x}) \neq 0\}$
$P(\boldsymbol{\alpha})$	Original pupil function
$M(\boldsymbol{x})$	Mask function
C	Constant factor in the mask function
$m(x)$	$1 - M(\boldsymbol{x})/C$
ϵ	Mask parameter
θ_*	Stellar angular radius
$L_{4\text{th}}(\boldsymbol{x}, \theta_*, \gamma)$	Leakage of light from the central star
$\tau_{4\text{th}}(\boldsymbol{\theta})$	Peak throughput
ζ_x, ζ_y	Constants that correspond to $\int_\infty^\infty d\alpha P(\boldsymbol{\alpha})$ and $\int_\infty^\infty d\beta P(\boldsymbol{\alpha})$ at $\text{Supp}[P]$
d	Distance from the target to the telescope
$\theta_{\text{sep}}(T_{\text{eff}})$	Angular separation of habitable planets normalized by λ/D
$\theta_*(T_{\text{eff}})$	Angular radii of host stars normalized by λ/D
$r_p(T_{\text{eff}})$	Geometric mean of the inner and outer edges of the habitable zone proposed by Kopparapu et al. (2013).

2.1. Concept

2.1.1. Band-limited Mask Coronagraph with Segmented Telescopes

First, we review the BLMC for preparation. We define the Cartesian coordinates, $\boldsymbol{\alpha} = (\alpha, \beta)$ on the pupil and $\boldsymbol{x} = (x, y)$ on the focal plane, respectively, see Figure 1. The coordinates are scaled to the imaging magnification and normalized by D_α or D_β and λ/D_α or λ/D_β, respectively. The mask function of the BLMC is generally written as

$$M(\boldsymbol{x}) = C(1 - m(x)), \tag{1}$$

where $m(x)$ satisfies $m(0) = 1 \leftrightarrow \int_{-\infty}^\infty d\alpha \tilde{m}(\alpha) = 1$. Also, C is a constant and is determined such as the following two requirements are satisfied: (i) $\lvert M(\boldsymbol{x}) \rvert \leqslant 1$ (the assumption that amplitude masks cannot amplify light) and (ii) C is as large as possible for higher throughput of the companion source (i.e.,
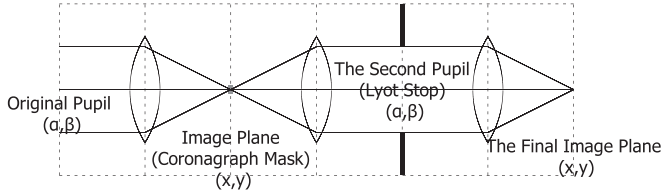
Figure 1. Cartesian coordinates scaled by the imaging magnification of the pupil and image planes. The coordinates are normalized by D and λ/D, respectively.

planet). The Fourier conjugate of $M(\boldsymbol{x})$ is

$$\tilde{M}(\boldsymbol{\alpha}) = C(\delta(\alpha)\delta(\beta) - \delta(\beta)\tilde{m}(\alpha)). \tag{2}$$

The second pupil amplitude is the convolution of $P(\boldsymbol{\alpha})$ and $\tilde{M}(\boldsymbol{\alpha})$:

$$P(\boldsymbol{\alpha}) * \tilde{M}(\boldsymbol{\alpha}) = C(P(\boldsymbol{\alpha}) - P(\boldsymbol{\alpha}) * \delta(\beta)\tilde{m}(\alpha)). \tag{3}$$

Therefore, to null the second pupil amplitude at the point, $\boldsymbol{\alpha}$, we require the following condition:

$$\mathrm{Supp}[\delta(\beta' - \beta)\tilde{m}(\alpha' - \alpha)] \in \mathrm{Supp}[P(\boldsymbol{\alpha'})], \tag{4}$$

where $\mathrm{Supp}[f(\boldsymbol{\alpha'})]$ means $\{\boldsymbol{\alpha'}|f(\boldsymbol{\alpha'}) \neq 0\}$. Considering Equation (4), the BLMC can null the second pupil amplitude over a wide range of pupils with a monolithic telescope without apodization (see panels (a)–(c) of Figure 2). However, the BLMC with a practical mask width over a segmented telescope cannot achieve a complete null on the second pupil due to the discontinuity of the segmented pupil (see panels (d)–(f) of Figure 2).

2.1.2. Concept of the New Coronagraph

To solve the above problem, we propose a new coronagraphic concept. Although the new mask type is an extension of the BLMC, the functional form and physical behavior of the new mask are qualitatively different from the BLMC (see Figure 3).

One of the BLMC mask patterns, $m(\boldsymbol{x}) = \frac{1}{\epsilon}\frac{\sin(\epsilon\pi x)}{\pi x}$, is the starting point for derivation of this concept, where ϵ is a real number. We choose this pattern because the $\tilde{m}(\boldsymbol{\alpha})$ is a rectangular function, $\frac{1}{\epsilon}\mathrm{rect}[\epsilon\alpha]$, where $\mathrm{rect}[\alpha]$ takes a constant value of 1 at $|\alpha| < 0.5$, 0.5 at $|\alpha| = 0.5$, and 0 at $0.5 < |\alpha|$. The other BLMC mask patterns are not to be used to derive the new coronagraph concept. The important point is that $P(\boldsymbol{\alpha}) * \tilde{m}(\boldsymbol{\alpha})$ is a constant over the original pupil aperture when the following two conditions are satisfied: (1) $\mathrm{Supp}[\tilde{m}]$ is two or more times wider than the original pupil aperture (see Figure 4(b)) and (2) $\int_{-\infty}^{\infty} d\alpha P(\boldsymbol{\alpha})\big/P(\boldsymbol{\alpha})$ is a constant (hereinafter referred to as ζ_x) at the original pupil aperture; for example, when the pupil is simply $\mathrm{rect}[\alpha]$, which has no gaps, ζ_x takes 1. When simply setting ϵ of the mask function of the BLMC to 2 or larger, the value of $P(\boldsymbol{\alpha}) * \tilde{m}(\boldsymbol{\alpha})$ on the original pupil aperture becomes a constant, ζ_x^{-1}. Since this constant is not 1, the pupil amplitude on the second pupil cannot be nulled.

However, by multiplying $m(\boldsymbol{x})$ by a constant factor such that the value of $P(\boldsymbol{\alpha}) * \tilde{m}(\boldsymbol{\alpha})$ is 1, the mask can null the pupil amplitude at the original pupil of the second pupil. Therefore, the solution to derive the new mask is a redefinition of $m(\boldsymbol{x})$ by

multiplying $\zeta_x^{-1}\epsilon$ for $m(\boldsymbol{x})$ above:

$$
\begin{aligned}
m_{\mathrm{new}}(\boldsymbol{x}) &= \zeta_x^{-1}\epsilon \times m(\boldsymbol{x}) \\
&= \zeta_x^{-1}\frac{\sin(\epsilon\pi x)}{\pi x}.
\end{aligned} \tag{5}
$$

Note that, hereafter in this paper, we use the symbol $m(\boldsymbol{x})$ to express the redefined one, $m_{\mathrm{new}}(\boldsymbol{x})$ for simplicity. At $\boldsymbol{x} = 0$, the value of the right-hand side of Equation (5) is $\zeta_x^{-1}\epsilon$, which is larger than 1. This leads to the negative value (π-radian phase shift) of the mask function, $C(1 - m(\boldsymbol{x}))$. This is fully different from the BLMC which includes only amplitude modulation. In Figure 4(c), we have that the pupil amplitude on the second pupil is exactly nulled using the new mask. Therefore, the Lyot stop is designed such that the aperture of the Lyot stop is exactly the same as the original pupil (Figure 4(d)). Also, since $\mathrm{Supp}[\tilde{m}(\alpha)]$ is two times wider than the original pupil aperture, the central peak of $m(\boldsymbol{x})$ is two times narrower than that of $\tilde{P}(x)$ (Figure 4(g)); therefore, we observe the planets that are closer to the host star. Furthermore, considering the focal plane, we can express the masked on-axis focal amplitude (see Figure 4(h)) by

$$C(1 - m(\boldsymbol{x}))\tilde{P}(\boldsymbol{x}) = C\left(1 - \zeta_x^{-1}\frac{\sin(\epsilon\pi x)}{\pi x}\right)\tilde{P}(\boldsymbol{x}). \tag{6}$$

Considering the different widths of the central peak of $m(\boldsymbol{x})$ and $\tilde{P}(x)$, the function of Equation (6) can be interpreted as a (upside down) wavelet whose Fourier conjugate (the second pupil function) has a non-zero value only outside the original pupil. Meanwhile, the off-axis focus amplitudes are not modulated into such wavelets by the new mask because the positions of those peaks do not match. Therefore, the mask can be said to selectively change the on-axis amplitude to a wavelet.

2.2. Fourth-order Null with a Hexagonally Segmented Telescope

It is known that, if we observe a nearby planetary system using a space telescope with a diameter of 5–10 m in optical and near-infrared wavelengths, then the second-order null is not sufficient since the angular radius of the target star is typically on the order of $10^{-2}\lambda/D$. Thus, we introduce a fourth-order null with the new mask. To obtain the fourth-order null, we consider the following two points. (1) Two successive new masks are assembled orthogonally to each other with an additional intermediate Lyot stop. In this paper, we use the y-dependent mask first, and then the x-dependent mask (Figure 5). (2) The pupil function before employing the focal plane mask must have rectangular aperture with optimized gaps as shown in Figure 6. Also, we required that all the Lyot stops should have the same apertures as the pupil function (Figure 5). The optimization of the gaps was carried out such that the pupil satisfies the requirement. The requirement is that both $\zeta_x = \int_{-\infty}^{\infty} d\alpha P(\boldsymbol{\alpha})\big/P(\boldsymbol{\alpha})$ and $\zeta_y = \int_{-\infty}^{\infty} d\beta P(\boldsymbol{\alpha})\big/P(\boldsymbol{\alpha})$ are constant at the original pupil aperture except for the region very close to the gap intersection. For adequate implementations, we eliminate the defects in areas very close to the gap intersection using a Lyot stop with a shield slightly wider than the gap of the original pupil. In this paper, we neglect little changes of the pupil stops, since these changes have little or no
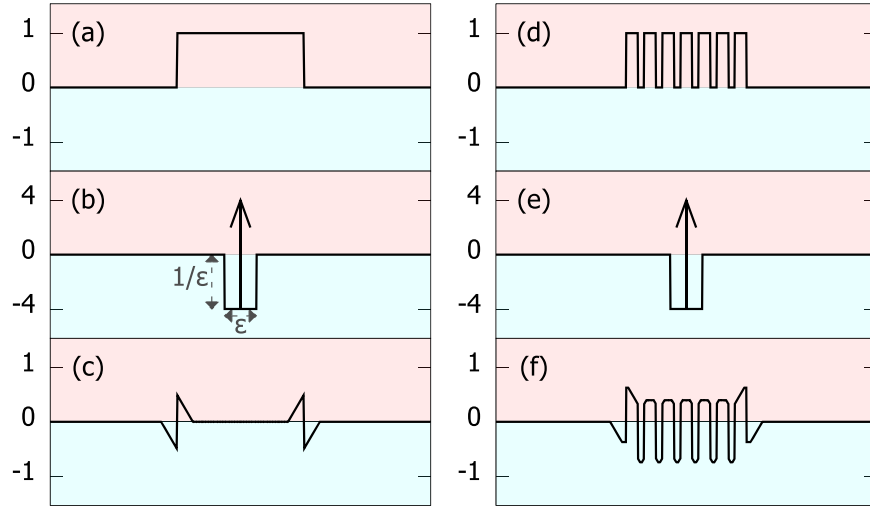
Figure 2. BLMC applied to monolithic (left column) and segmented (right column) telescopes. Each horizontal line represents zero amplitude and the vertical upward arrow represents the delta function. (a) A pupil function of a monolithic telescope. (b) Fourier conjugate of the BLMC mask function. (c) The second pupil amplitude (the convolution of (a) and (b)). (d) A discontinuous pupil function of a segmented telescope. (e) Fourier conjugate of the BLMC mask function. (f) The second pupil amplitude (the convolution of (d) and (e)).

impact on the performance of the new mask. The derivation of expressions for the performance of the fourth-order system is complied in the Appendix.

The stellar leakage of the fourth-order new mask (normalized by the original intensity of the stellar light) is expressed as

$$
\begin{aligned}
L_{4\mathrm{th}}(\boldsymbol{x},\,\theta_*,\,\gamma) = C^4 &\left\{ \left(\frac{\partial^2}{\partial x \partial y} \tilde{P}(\boldsymbol{x}) \right)^2 \right. \\
&\times \left(\frac{1}{24}\theta_*^4 + \frac{1}{4}\theta_*^2\gamma^2 + \frac{1}{4}\gamma^4 \right) \\
&+ \left(\frac{\partial^2}{\partial x \partial y}\tilde{P}(\boldsymbol{x}) \right) A(\boldsymbol{x}) \left(\frac{3}{8}\theta_*^2\gamma^2 \right) \\
&\left. + A(\boldsymbol{x})^2 \left(\frac{1}{32}\theta_*^4 + \frac{3}{16}\theta_*^2\gamma^2 + \frac{3}{16}\gamma^4 \right) \right\},
\end{aligned}
\tag{7}
$$

where θ_* is the stellar angular radius, γ is the normalized angles of the telescope pointing jitter, and

$$
\begin{aligned}
A(\boldsymbol{x}) = 4\pi^2 \zeta_y^{-1} \int_{-\infty}^{\infty} d\boldsymbol{\alpha}\, e^{-2\pi i \boldsymbol{x}\cdot\boldsymbol{\alpha}} P(\boldsymbol{\alpha}) \\
\times \left(1 - \zeta_x^{-1} \int_{-\infty}^{\infty} d\alpha \right) P(\boldsymbol{\alpha}) \int_{-\infty}^{\infty} d\beta \beta^2 P(\boldsymbol{\alpha}).
\end{aligned}
\tag{8}
$$

The azimuth angle of the tilt direction is set with an uniform distribution of $[0, 2\pi]$, and Equation (7) represents the average leakage with respect to the azimuth. Due to the presence of the intermediate Lyot stop, the leak is not symmetric with respect to the exchange of x and y.

The planetary peak throughput is different from the profile of the mask function because a new mask introduces π-radian phase modulation. Figure 7 shows the planetary peak throughput of the fourth-order new mask. This peak throughput
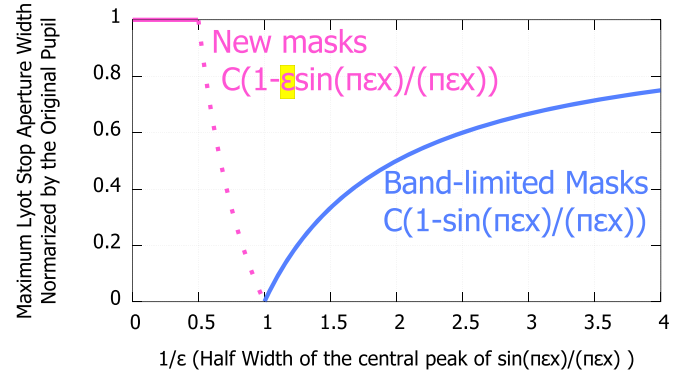

Figure 3. Difference between the new mask and the BLMC (maximum possible aperture width of the Lyot stop as a function of the width of the second term of the mask function). For simplicity, the discussion is limited to one-dimension, and the original pupil function is assumed to be rect[α] in this figure. The width of the original pupil is 1. When $\epsilon^{-1} = 1$, the width of the second term of the mask function and stellar diffraction amplitude are the same. Note that the functional form at $0 \leqslant \epsilon^{-1} < 1$ (the new mask, magenta line) and at $1 \leqslant \epsilon^{-1}$ (the BLMC, blue line) differ. The maximum width of the Lyot stop aperture is the same as the original pupil when $\epsilon^{-1} \leqslant 0.5$ (solid magenta line). The "ϵ" at the beginning of the second term of the new mask function works to add π-radian phase modulation onto the stellar diffraction amplitude.

is evaluated using

$$
\tau_{4\mathrm{th}}(\boldsymbol{\theta}) = C^4 \left(\left(1 - \left(\frac{\sin(\epsilon\pi x)}{\pi x} \right)^2 \right) \left(1 - \left(\frac{\sin(\epsilon\pi y)}{\pi y} \right)^2 \right) \right)^2.
\tag{9}
$$

And since the impact small, we neglect the effect of the pupil gaps on the throughput. The effect of the obscuration is neglected in Equation (9), see Figure 6, and Figure 7 shows the result. Although such light loss independent on $\boldsymbol{\theta}$ degrades the ratio of the signal to the photon noise, it does not affect the ratio of planetary signals to stellar leaks at all. If we neglect such constant factors, then the profile of the peak throughput is close to the theoretical limit proposed by Guyon et al. (2006).
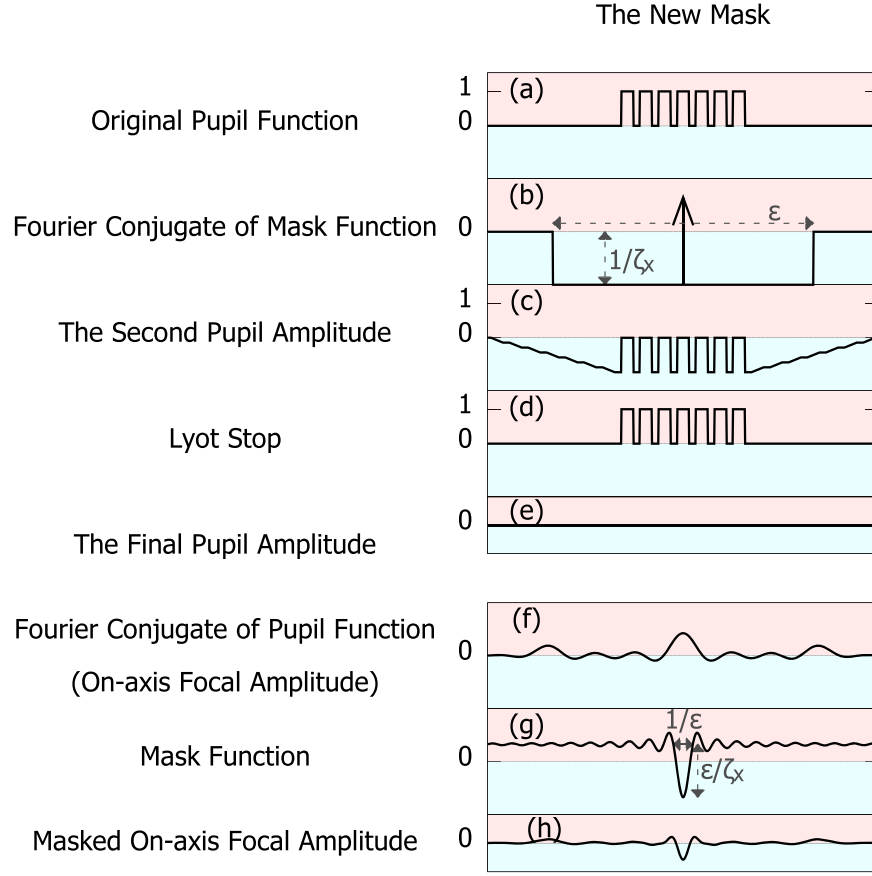
The New Mask

Figure 4. Concept of the new mask. Each horizontal line represents zero amplitude and the vertical upward arrow represents the delta function. The constant factor, C, is omitted in this figure. (a) A discontinuous pupil function of a segmented telescope. (b) Fourier conjugate of the new coronagraphic mask function. (c) The second pupil amplitude (the convolution of (a) and (b)). (d) Lyot stop aperture function. (e) The final pupil amplitude. (f) Fourier conjugate of the pupil function (on-axis focal amplitude before masking). (g) The new function. (h) Amplitude of an on-axis source modulated by the new mask on the focal plane (the product of (f) and (g)).

3. Simulation

In this section, the performance of a fourth-order coronagraphic system with an unobscured off-axis segmented telescope is studied and discussed in terms of the detection of potentially habitable planets. We carried out the calculation using the analytical expressions of Equations (7) and (9). We consider the monochromatic light of 0.75 μm and a primary mirror the same as that of the LUVOIR-b architecture.

3.1. Assumptions

In the simulation, the normalized angular separation between the planet and its host star and the normalized stellar angular radius with λ/D, $\theta_{\rm sep}(T_{\rm eff})$ and $\theta_*(T_{\rm eff})$, are assumed as

$$\theta_{\rm sep}(T_{\rm eff}) = \frac{r_p(T_{\rm eff})}{d}/(\lambda/D) \qquad (10)$$

$$\theta_*(T_{\rm eff}) = \frac{R_*(T_{\rm eff})}{d}/(\lambda/D), \qquad (11)$$

where $r_p(T_{\rm eff})$ is the geometric mean of the inner and outer edges of the habitable zone proposed by Kopparapu et al. (2013) and d is the distance from a target to the telescope. Considering the LUVOIR-b architecture as the telescope used for this simulation, λ and D are set to 0.75 μm and 6.4 m, respectively. In Figure 6, we observe that the pupil effective diameter was reduced to 6.4 m from the original effective

diameter of LUVOIR-b, 8.5 m. The $R_*(T_{\rm eff})$ is the host star radius as a function of the effective temperature. We used the empirical relation of Boyajian et al. (2012) for this function. Then, we determine the contrast between the stellar and planetary light (Traub & Oppenheimer 2010) as

$$({\rm Contrast}) = \frac{0.367}{\pi}\left(\frac{R_\oplus}{r_p}\right)^2, \qquad (12)$$

where a face-on planet with a radius of $R_\oplus$ was considered.

3.2. Results

Figure 8 shows the normalized planetary signal by the original stellar intensity (i.e., the contrast multiplied by the peak throughput), $S(T_{\rm eff})$, and the stellar leakage, $L(T_{\rm eff})$. The results in Figure 8 were obtained using Equations (13) and (14),

$$S(T_{\rm eff}) = ({\rm Contrast}) \times \tau_{\rm 4th}\left(\frac{\theta_{\rm sep}(T_{\rm eff})}{\sqrt{2}}, \frac{\theta_{\rm sep}(T_{\rm eff})}{\sqrt{2}}\right) \qquad (13)$$

$$L(T_{\rm eff}) = L_{\rm 4th}\left(\frac{\theta_{\rm sep}(T_{\rm eff})}{\sqrt{2}}, \frac{\theta_{\rm sep}(T_{\rm eff})}{\sqrt{2}}, \theta_*(T_{\rm eff}), \gamma\right), \qquad (14)$$

where $\tau_{\rm 4th}(\boldsymbol{\theta})$ and $L_{\rm 4th}(\boldsymbol{\theta})$ are respectively as defined in Equations (9) and (7). The result shows the principle limitation of this coronagraphic performance for monochromatic light of 0.75 μm; the higher-order aberration of the telescope pointing
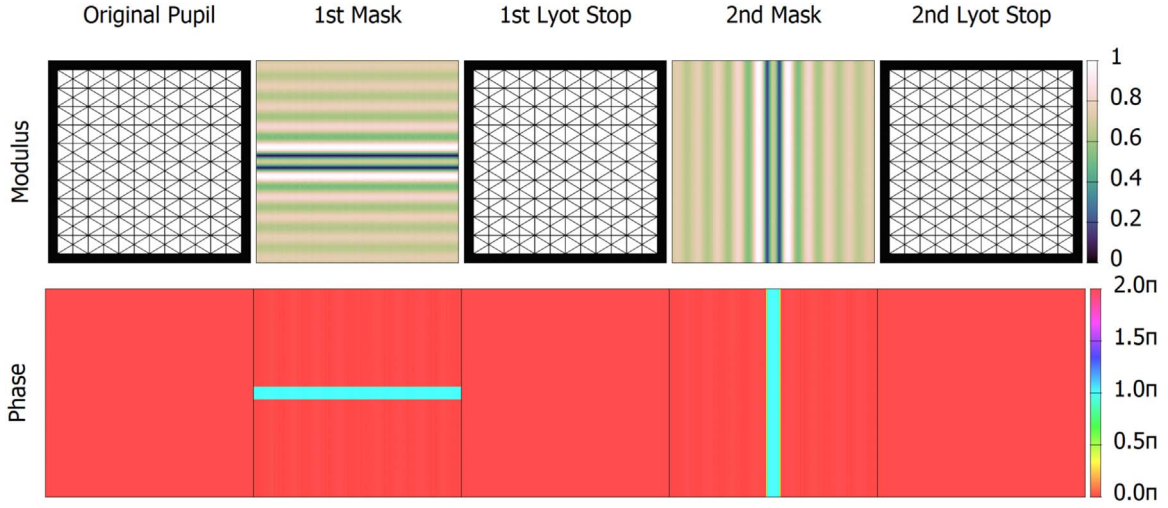
Figure 5. Modulus and phase of the pupil and focus masks used in a fourth-order coronagraphy system. The original pupil in the figure is obtained by the procedure shown in Figure 6. Two successive new masks are assembled orthogonally to each other with an additional intermediate Lyot stop. The first focus mask is the y-dependent mask and the second is the x-dependent mask.
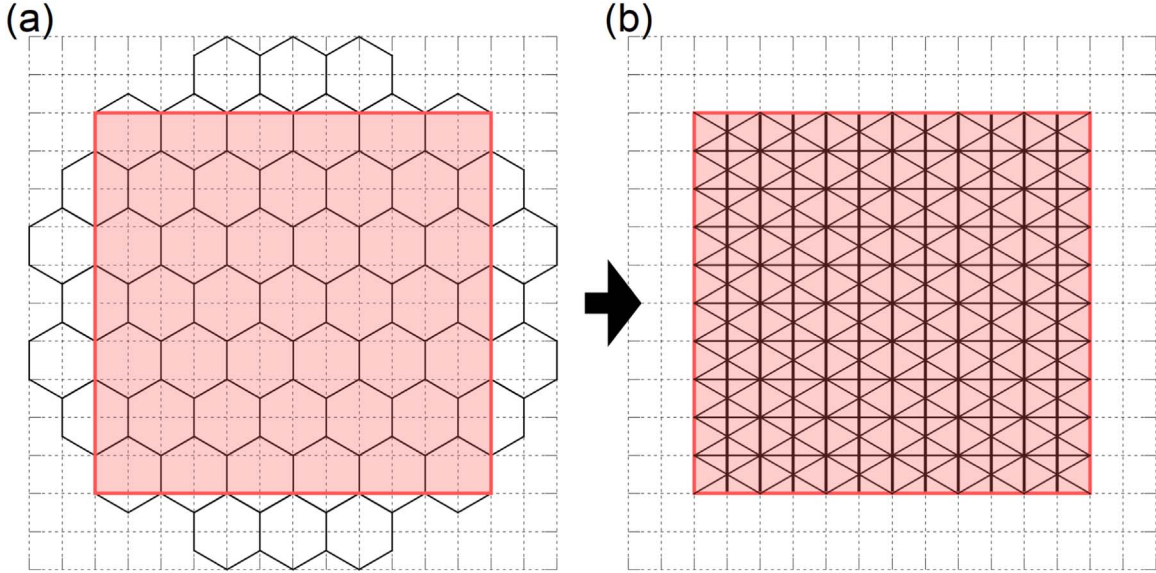

Figure 6. Procedure for making a rectangular pupil optimized for the new coronagraph. (a) Pupil function of the LUVOIR-b architecture. (b) Optimized pupil function.

jitter was not considered. The direction of $x = y$ on the image plane was chosen so that the throughput of the planetary signal becomes the largest (see Figure 7). The multiple peak structures in the plots of the stellar leak is caused by $\left(\frac{\partial^2}{\partial x \partial y} \tilde{P}(x)\right)^2$ in Equation (7). For polychromatic light, the multiple peaks would vanish because the variables of $\left(\frac{\partial^2}{\partial x \partial y} \tilde{P}(x)\right)^2$ are normalized by λ/D. The stellar leakage for the pointing jitter of $0.001\lambda/D$ is not different from the case of $0.01\lambda/D$ compared to the difference between the cases of $0.01\lambda/D$ and $0.1\lambda/D$. This is because the finite stellar angular radius is typically around $0.01\lambda/D$. Under the condition that the telescope pointing jitter is $0.001\lambda/D \approx 24\,\mu$as, the stellar leakage can be suppressed down to the planetary signal for all types of host stars (3200–5800 K) and distances (3, 5, and 10 pc). Even for the pointing jitter of $0.01\lambda/D$, the stellar leakage is

approximately less than or equal to the signals of the planets orbiting M-type stars at 3 pc, K-type stars at 5 pc, and G-type stars at 10 pc. Therefore, this fourth-order coronagraphic system is very effective for detecting the nearby terrestrial planets orbiting G-, K-, and potentially M-type stars.

4. Discussion

4.1. Broadband Imaging

This coronagraphic system should be optimized for a wide observing wavelength range. However, there is a problem with enlarging its wavelength range because the physical (unnormalized) scale of the point-spread function is proportional to the wavelength of the light. In other words, the profile of the focal plane mask should be scaled by the size of the point-spread function. This means that the performance of the new coronagraph system is largely degraded for broadband
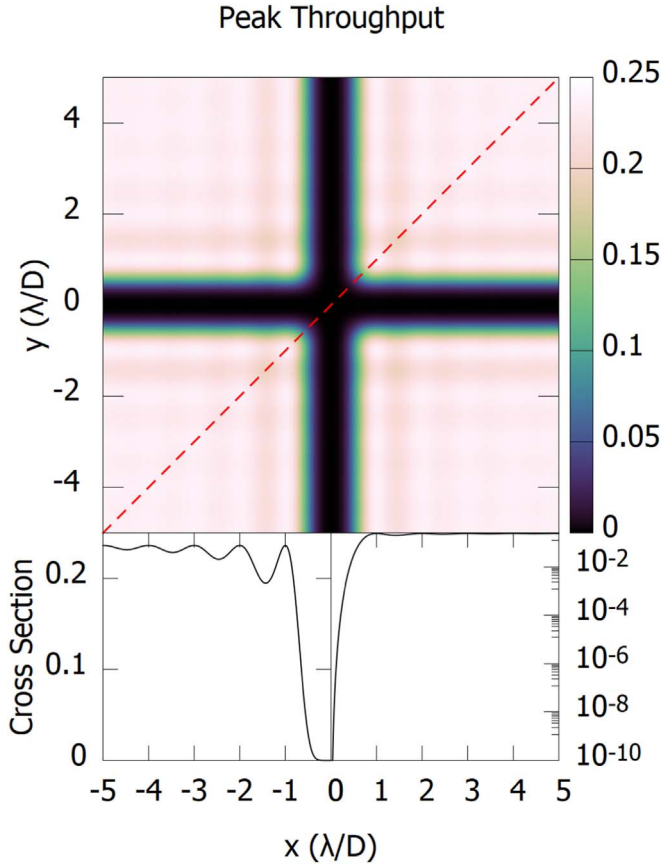
Peak Throughput

Figure 7. Peak throughput of the fourth-order new coronagraph at the off-axis angle ($\epsilon = 2$). The lower panel indicates the cross-section along the red dashed line ($x = y$) in the upper panel; the lower left and right panels are shown in linear and logarithm. The effect of the constant factor C^4 (≈ 0.25) is included. The effect of the pupil function (shown in Figure 6) on the throughput is not considered.

imaging. To estimate the impact of this factor, we make the following assumption. Although the mask is designed for the wavelength of λ, the actual wavelength is $\lambda + \Delta\lambda$, where $\frac{\Delta\lambda}{\lambda}$ is sufficiently smaller than 1. In this case, the spatial scale of the mask function (Figure 4, panel (g)) is magnified by $\frac{\lambda}{\lambda + \Delta\lambda}$ from the appropriate scale. Therefore, non-zero values of the Fourier conjugate of the mask function (Figure 4, panel (b)), excluding the central delta function peak, are scaled by $\frac{\lambda}{\lambda + \Delta\lambda} \approx 1 - \left(\frac{\Delta\lambda}{\lambda}\right)$ from the appropriate value. Hence, the remaining modulus of the amplitude on the second pupil is constant over the original pupil and is approximately estimated as $\left(\frac{\Delta\lambda}{\lambda}\right)$. For the fourth-order version, the remaining modulus of the amplitude on the last pupil becomes the square of the second-order version, $\left(\left(\frac{\Delta\lambda}{\lambda}\right)\right)^2 = \left(\frac{\Delta\lambda}{\lambda}\right)^2$. Thus, the leaks caused by the deviation of the wavelength are obtained as $\left(\frac{\Delta\lambda}{\lambda}\right)^4$ times the point-spread function before the coronagraphic system. This means that $\frac{\Delta\lambda}{\lambda}$ must be smaller than 0.32% for the contrast of 10^{-10}. Hence, we desire a method for implementing an achromatic new mask.

4.2. Prospects for Manufacturing

We also discuss the prospects for manufacturing the pupil stops and focal plane masks of the new coronagraph.

We assume that the manufacturing errors of the first pupil stop size and the first Lyot stop size are σ_1 and σ_2 in their standard deviation; these errors are normalized by the pupil full width. In this case, the on-axis source leakage caused by the manufacturing errors is proportional to $\sigma_1^2 \sigma_2^2$, where the errors are assumed to be the Gaussian distributions independent of each other. Therefore, we estimate the manufacturing tolerance for the pupil stop size to be $10^{-10/4} \approx 0.3\%$ of the pupil full width when aiming at the contrast of 10^{-10}.

We also assume that the manufacturing errors of the first and second focal plane masks in terms of amplitude transmittance are $e_1(\boldsymbol{x})$ and $e_2(\boldsymbol{x})$, respectively. We cannot simply estimate the resultant leakage of the fourth-order coronagraphic system at each point on the focal plane, $|e(\boldsymbol{x})|^2$, since it depends on the functional forms of $e_1(\boldsymbol{x})$ and $e_2(\boldsymbol{x})$. However, the upper limit of $\iint_{-\infty}^{\infty} d\boldsymbol{x}\, |e(\boldsymbol{x})|^2$ is obtained as

$$\iint_{-\infty}^{\infty} d\boldsymbol{x}\, |e(\boldsymbol{x})|^2 \leqslant \prod_i \iint_{-\infty}^{\infty} d\boldsymbol{x}\, |e_i(\boldsymbol{x})|^2. \qquad (15)$$

In the actual manufacturing, the focal plane masks of the new coronagraph are made as notch filter masks (Kuchner & Spergel 2003; Debes et al. 2004). This is because the notch filter mask is one of the binary masks whose Fourier conjugate is equal to the Fourier conjugate of the band-limited mask in the region two times wider than the Lyot stop. The difference between these Fourier conjugates has no impact on the convolution in Equation (3).

5. Conclusion

In this paper, we proposed a coronagraphic system with fourth-order null suitable for off-axis unobscured segmented telescopes. The coronagraphic system is comprised of a new type of focal plane mask and a Lyot stop that is almost the same as the original pupil. The new system is sufficiently insensitive to the telescope pointing errors and the finite host-star angular diameter thanks to the fourth-order null of the host star. Also, this coronagraphic system can suppress the stellar halo over a wide range of angular separations. The inner working angle is close to $1\lambda/D$ and there are no outer limits. The Fourier conjugate of the new mask function is the sum of the delta function and -1 times the rectangular function that has twice the width of the original pupil. Therefore, despite the application of the coronagraphic system to an off-axis unobscured segmented telescope, we can null the amplitude at the re-imaged pupil. The new coronagraph achieves the second-order null. The fourth-order version of the new coronagraph is constructed by placing two new masks in succession to be orthogonal to each other. We studied and investigated the performance of this fourth-order band-limited mask coronagraph for observations in monochromatic $\lambda = 0.75\,\mu\text{m}$ light with an 8.5 m segmented telescope. According to the result, potentially habitable planets around nearby G- and K-type main-sequence stars can be directly detected for the pointing jitter less than $0.01\lambda/D$ or less of the pointing jitter.

We estimated the limited bandwidth due to the contrast of 10^{-10}; $\frac{\Delta\lambda}{\lambda}$ must be smaller than 0.32% for the contrast of 10^{-10}. The manufacturing tolerance for the pupil stop size is $10^{-10/4} \approx 0.3\%$ of the pupil full width for the contrast of 10^{-10}. The focal plane masks of the new coronagraph would be possibly made as notch filter masks. However, further investigation of this mask is highly encouraged to make an absolute statement. The new coronagraph mask concept is
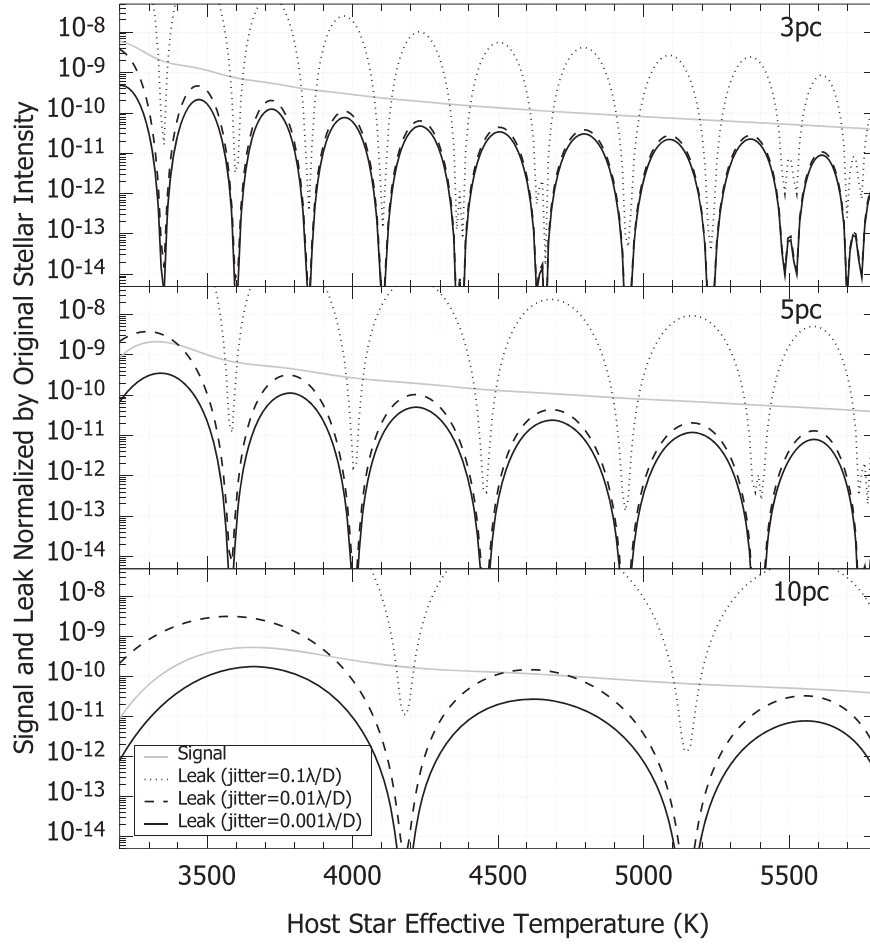
Figure 8. Normalized signals of a terrestrial planet in the habitable zone by the original stellar intensity (i.e., a product of the contrast between the planet and its host star and the peak throughput) and the stellar leak as a function of various stellar effective temperatures. The distances from the targets to the telescope are set to 3 (top), 5 (center), and 10 pc (bottom). The gray solid line shows the planetary signal. The black dotted, dashed, and solid lines indicate the stellar leak for the telescope pointing jitter of 0.1, 0.01, and 0.001 λ/D, respectively.

effective for the direct imaging of potentially habitable planets with the future space off-axis segmented telescopes.

Appendix
Derivation of Expressions for the Performance of the Fourth-order System

This appendix derives the characteristics of the fourth-order coronagraph system proposed in Section 2.2. In the following, the aperture function of the pupil just before the focal plane mask and the first and second Lyot stops are denoted as $P_1(\boldsymbol{\alpha})$, $P_2(\boldsymbol{\alpha})$, and $P_3(\boldsymbol{\alpha})$ respectively. The values of these aperture functions can be 1 or 0. The following is assumed:

$$P_2(\boldsymbol{\alpha}) = P_2(\boldsymbol{\alpha})P_1(\boldsymbol{\alpha}), \tag{A1}$$

$$P_3(\boldsymbol{\alpha}) = P_3(\boldsymbol{\alpha})P_2(\boldsymbol{\alpha})P_1(\boldsymbol{\alpha}). \tag{A2}$$

Additionally, the first and second masks, $M_y(\boldsymbol{x})$ and $M_x(\boldsymbol{x})$, are defined as

$$M_y(\boldsymbol{x}) = C\left(1 - \zeta_y^{-1}\frac{\sin(\epsilon \pi y)}{\pi y}\right), \tag{A3}$$

$$M_x(\boldsymbol{x}) = C\left(1 - \zeta_x^{-1}\frac{\sin(\epsilon \pi x)}{\pi x}\right), \tag{A4}$$

where $2 \leqslant \epsilon$. In the following, the variables of these functions such as $\boldsymbol{\alpha}$ or $\boldsymbol{x}$ are sometimes omitted for notational simplicity.

We first derive the point-spread function for the fourth-order coronagraph system for preparation. The point-spread function that depends on the position angle of the point source, $\boldsymbol{\theta}$, can be derived as

$$\mathrm{PSF}(\boldsymbol{x}, \boldsymbol{\theta})$$
$$= C^4 \left| \int_{-\infty}^{\infty} d\boldsymbol{\alpha}\, e^{-2\pi i \boldsymbol{x}\cdot\boldsymbol{\alpha}} P_3(\tilde{M}_x * (P_2(\tilde{M}_y * (P_1 e^{2\pi i \boldsymbol{\theta}\cdot\boldsymbol{\alpha}})))) \right|^2$$
$$= C^4 \left| \int_{-\infty}^{\infty} d\boldsymbol{\alpha}\, e^{-2\pi i \boldsymbol{x}\cdot\boldsymbol{\alpha}} P_3\left(1 - \zeta_x^{-1}\int_{-\infty}^{\infty} d\alpha\right) \right.$$
$$\left. \times P_2\left(1 - \zeta_y^{-1}\int_{-\infty}^{\infty} d\beta\right) P_1 e^{2\pi i \boldsymbol{\theta}\cdot\boldsymbol{\alpha}} \right|^2. \tag{A5}$$

When $P_1 = P_2 = P_3 = \mathrm{rect}[\alpha]\mathrm{rect}[\beta]$, $\mathrm{PSF}(\boldsymbol{x}, \boldsymbol{\theta})$ can be simply expressed by

$$\mathrm{PSF}(\boldsymbol{x}, \boldsymbol{\theta}) = \mathrm{PSF}_{1-D}(x, \theta_x)\mathrm{PSF}_{1-D}(y, \theta_y), \tag{A6}$$

where

$$\mathrm{PSF}_{1-D}(x, \theta_x)$$
$$= C^2 \left| \left(\frac{\sin(\epsilon\pi(x - \theta_x))}{\pi(x - \theta_x)} - \frac{\sin(\epsilon\pi x)}{\pi x} \frac{\sin(\epsilon\pi\theta_x)}{\pi\theta_x} \right) \right|^2 .$$

(A7)

A.1. Peak Throughput

To derive the peak throughput of the system, substitute $x = \theta$ into Equations (A6) and (A7):

$$\tau_{4\mathrm{th}}(\boldsymbol{\theta}) = \mathrm{PSF}(\boldsymbol{\theta}, \boldsymbol{\theta})$$
$$= C^4 \left| \left(1 - \left(\frac{\sin(\epsilon\pi\theta_x)}{\pi\theta_x} \right)^2 \right) \left(1 - \left(\frac{\sin(\epsilon\pi\theta_y)}{\pi\theta_y} \right)^2 \right) \right|^2 .$$

(A8)

A.2. Leak of Stellar Light

In the following, we assume

$$P_3 = P_2 = P_1 = P$$

(A9)

for simplicity. P is a real function thus $\tilde{P}$ is an even function. Using this fact, Taylor expansion of $\mathrm{PSF}(\boldsymbol{x}, \boldsymbol{\theta})$ about $\boldsymbol{\theta}$ around $\boldsymbol{\theta} = 0$ can be calculated as

$$\mathrm{PSF}(\boldsymbol{x}, \boldsymbol{\theta}) = C^4 \left(A_{xy}(\boldsymbol{x})^2 \theta_x^2 \theta_y^2 \right.$$
$$\left. + A_{xy}(\boldsymbol{x}) A_{yy}(\boldsymbol{x}) \theta_x \theta_y^3 + \frac{A_{yy}(\boldsymbol{x})^2}{4} \theta_y^4 \right),$$

(A10)

where terms of an order higher than 4 are ignored. In Equation (A10), A_{xy} and A_{yy} are defined as

$$A_{xy}(\boldsymbol{x}) = \frac{\partial^2}{\partial x \partial y} \tilde{P}(\boldsymbol{x}),$$

(A11)

$$A_{yy}(\boldsymbol{x}) = 4\pi^2 \zeta_y^{-1} \int_{-\infty}^{\infty} d\boldsymbol{\alpha} e^{-2\pi i \boldsymbol{x} \cdot \boldsymbol{\alpha}} P(\boldsymbol{\alpha})$$
$$\times \left(1 - \zeta_x^{-1} \int_{-\infty}^{\infty} d\alpha \right) P(\boldsymbol{\alpha}) \int_{-\infty}^{\infty} d\beta \beta^2 P(\boldsymbol{\alpha}).$$

(A12)

We use Equation (A10) and the following expression to calculate the stellar leakage of the fourth-order new mask (normalized by the original intensity of the stellar light):

$$L_{4\mathrm{th}}(\boldsymbol{x}, \theta_*, \gamma) = \frac{1}{2\pi} \int_0^{2\pi} d\Phi \frac{1}{\pi \theta_*^2} \int_0^{\theta_*} \theta d\theta$$
$$\times \int_0^{2\pi} d\phi \mathrm{PSF}(\boldsymbol{x}, \boldsymbol{\theta} - \boldsymbol{\gamma}),$$

(A13)

where $\boldsymbol{\gamma}$ means pointing jitter,

$$\boldsymbol{\gamma} = (\gamma \cos(\Phi), \gamma \sin(\Phi)),$$

(A14)

and the operator, $\frac{1}{2\pi} \int_0^{2\pi} d\Phi$, expresses the average with respect to the azimuth, Φ. To calculate the right-hand side of

Equation (A13), we define the following definite integrals:

$$L_{nm} = \int_0^{2\pi} d\phi (\cos(\phi))^n (\sin(\phi))^m,$$

(A15)

where n and m are integers. When both n and m are even numbers,

$$L_{nm} = L_{mn}$$
$$= 2^{1-n-m} \pi \sum_{k=0}^{n} \binom{n}{k} \binom{m}{\frac{n+m}{2} - k} (-1)^k.$$

(A16)

When either n or m are odd numbers,

$$L_{nm} = 0.$$

(A17)

The values for even (n, m) up to 4 are

$$(L_{00}, L_{20}, L_{22}, L_{40}) = \left(2\pi, \pi, \frac{\pi}{4}, \frac{3\pi}{4} \right).$$

(A18)

Using these definite integrals, the right-hand side of Equation (A13) can be calculated as

$$L_{4\mathrm{th}}(\boldsymbol{x}, \theta_*, \gamma) = \frac{C^4}{\pi\theta_*^2} \frac{1}{2\pi} \int_0^{2\pi} d\Phi \int_0^{\theta_*} \theta d\theta \left\{ A_{xy}(\boldsymbol{x})^2 \right.$$
$$\times (L_{22}\theta^4 + L_{20}\theta^2\gamma^2 + L_{00}\gamma_x^2\gamma_y^2)$$
$$+ A_{xy}(\boldsymbol{x}) A_{yy}(\boldsymbol{x})(3L_{02}\theta^2\gamma_x^2 + L_{00}\gamma_x\gamma_y^3)$$
$$\left. + \frac{1}{4} A_{yy}(\boldsymbol{x})^2 (L_{04}\theta^4 + 6L_{02}\theta^2\gamma_y^2 + L_{00}\gamma_y^4) \right\}$$
$$= C^4 \frac{1}{2\pi} \int_0^{2\pi} d\Phi \left\{ A_{xy}(\boldsymbol{x})^2 \right.$$
$$\times \left(\frac{1}{24}\theta_*^4 + \frac{1}{4}\gamma^2\theta_*^2 + \gamma_x^2\gamma_y^2 \right)$$
$$+ A_{xy}(\boldsymbol{x}) A_{yy}(\boldsymbol{x}) \left(\frac{3}{4}\theta_*^2\gamma_x^2 + \gamma_x\gamma_y^3 \right)$$
$$\left. + A_{yy}(\boldsymbol{x})^2 \left(\frac{1}{32}\theta_*^4 + \frac{3}{8}\theta_*^2\gamma_y^2 + \frac{1}{4}\gamma_y^4 \right) \right\}$$
$$= C^4 \left\{ A_{xy}(\boldsymbol{x})^2 \left(\frac{1}{24}\theta_*^4 + \frac{1}{4}\gamma^2\theta_*^2 + \gamma^4\frac{L_{22}}{2\pi} \right) \right.$$
$$+ A_{xy}(\boldsymbol{x}) A_{yy}(\boldsymbol{x}) \left(\frac{3}{4}\theta_*^2\gamma^2\frac{L_{02}}{2\pi} \right)$$
$$\left. + A_{yy}(\boldsymbol{x})^2 \left(\frac{1}{32}\theta_*^4 + \frac{3}{8}\theta_*^2\gamma^2\frac{L_{02}}{2\pi} + \frac{1}{4}\gamma^4\frac{L_{04}}{2\pi} \right) \right\}$$
$$= C^4 \left\{ A_{xy}(\boldsymbol{x})^2 \left(\frac{1}{24}\theta_*^4 + \frac{1}{4}\gamma^2\theta_*^2 + \frac{1}{4}\gamma^4 \right) \right.$$
$$+ A_{xy}(\boldsymbol{x}) A_{yy}(\boldsymbol{x}) \left(\frac{3}{8}\theta_*^2\gamma^2 \right)$$
$$\left. + A_{yy}(\boldsymbol{x})^2 \left(\frac{1}{32}\theta_*^4 + \frac{3}{16}\theta_*^2\gamma^2 + \frac{3}{16}\gamma^4 \right) \right\}.$$

(A19)

ORCID iDs

Satoshi Itoh ⓘ https://orcid.org/0000-0003-2690-7092

References

Angel, J. R. P., Cheng, A. Y. S., & Woolf, N. J. 1986, Natur, 322, 341
Angel, J. R. P., & Woolf, N. J. 1997, ApJ, 475, 373
Anglada-Escudé, G., Amado, P. J., Barnes, J., et al. 2016, Natur, 536, 437
Belikov, R., Bryson, S., Sirbu, D., et al. 2018, Proc. SPIE, 10698, 106981H
Bolcar, M. R., Crooke, J., Hylan, J. E., et al. 2018, Proc. SPIE, 10698, 106980O
Borucki, W. J. 2017, PAPhS, 161, 38
Boyajian, T. S., von Braun, K., van Belle, G., et al. 2012, ApJ, 757, 112
Bracewell, R. N., & MacPhie, R. H. 1979, Icar, 38, 136
Cash, W. 2006, Natur, 442, 51
Catling, D. C., Krissansen-Totton, J., Kiang, N. Y., et al. 2018, AsBio, 18, 709
Copi, C. J., & Starkman, G. D. 2000, ApJ, 532, 581
Debes, J. H., Ge, J., Kuchner, M. J., & Rogosky, M. 2004, ApJ, 608, 1095
Foo, G., Palacios, D. M., & Swartzlander, G. A., Jr. 2005, OptL, 30, 3308
Fujii, Y., Angerhausen, D., Deitrick, R., et al. 2018, AsBio, 18, 739
Gillon, M., Jehin, E., Lederer, S. M., et al. 2016, Natur, 533, 221
Goda, S., & Matsuo, T. 2018, AJ, 156, 288
Gong, Q., Bolcar, M. R., Corsetti, J. A., et al. 2019, JATIS, 5, 025002
Guyon, O., Martinache, F., Belikov, R., & Soummer, R. 2010, ApJS, 190, 220
Guyon, O., Pluzhnik, E. A., Galicher, R., et al. 2005, ApJ, 622, 744
Guyon, O., Pluzhnik, E. A., Kuchner, M. J., Collins, B., & Ridgway, S. T. 2006, ApJS, 167, 81
Hicks, B. A., Lyon, R. G., Petrone, P., et al. 2016, Proc. SPIE, 9904, 990420
Howard, A. W., Marcy, G. W., Bryson, S. T., et al. 2012, ApJS, 201, 15
Itoh, S., Matsuo, T., Goda, S., Shibai, H., & Sumi, T. 2017, AJ, 154, 97
Kaltenegger, L. 2017, ARA&A, 55, 433
Kiang, N. Y., Domagal-Goldman, S., Parenteau, M. N., et al. 2018, AsBio, 18, 619
Kopparapu, R. K., Ramirez, R., Kasting, J. F., et al. 2013, ApJ, 765, 131
Kuchner, M. J., & Spergel, D. N. 2003, ApJ, 594, 617
Kuchner, M. J., & Traub, W. A. 2002, ApJ, 570, 900
Leisawitz, D., Amatucci, E., Carter, R., et al. 2018, Proc. SPIE, 10698, 1069815
Matsuo, T., Itoh, S., Shibai, H., Sumi, T., & Yamamuro, T. 2016, ApJ, 823, 139
Matsuo, T., Traub, W. A., Hattori, M., & Tamura, M. 2011, ApJ, 729, 50
Mawet, D., Riaud, P., Absil, O., & Surdej, J. 2005, ApJ, 633, 1191
Mazoyer, J., Baudoz, P., Belikov, R., et al. 2019, BAAS, 51, 101
Meadows, V. S., Reinhard, C. T., Arney, G. N., et al. 2018, AsBio, 18, 630
N'Diaye, M., Soummer, R., Pueyo, L., et al. 2016, ApJ, 818, 163
Ricker, G. R., Winn, J. N., Vanderspek, R., et al. 2015, JATIS, 1, 014003
Roddier, F., & Roddier, C. 1997, PASP, 109, 815
Rouan, D., Riaud, P., Boccaletti, A., Clénet, Y., & Labeyrie, A. 2000, PASP, 112, 1479
Ruane, G., Mawet, D., Mennesson, B., Jewell, J., & Shaklan, S. 2018, JATIS, 4, 015004
Schwieterman, E. W., Kiang, N. Y., Parenteau, M. N., et al. 2018, AsBio, 18, 663
Sivaramakrishnan, A., & Yaitskova, N. 2005, ApJL, 626, L65
Soummer, R. 2005, ApJL, 618, L161
Traub, W. A., & Oppenheimer, B. R. 2010, in Exoplanets, ed. S. Seager (Tucson, AZ: Univ. Arizona Press), 111
Vanderbei, R. J., Cady, E., & Kasdin, N. J. 2007, ApJ, 665, 794